ACS OMEGA

http://pubs.acs.org/journal/acsodf

Article

Universal Water Disinfection by the Introduction of Fe−N_3 Traps between g-C_3N_4 Layers under Visible Light

Ling Pu, Jiying Wang, Zhao Hu,* and Yujiao Zhang*

Cite This: *ACS Omega* 2023, 8, 27276−27283

Read Online

ACCESS | Metrics & More | Article Recommendations | Supporting Information

ABSTRACT: Efficient inactivation of bacteria in the sewage via a photocatalytic process represents a promising strategy for the efficient chemical utilization of solar energy. Herein, uniformly dispersed Fe atoms were embedded between layers of g-C_3N_4 photocatalysts (CNF*x*), which were facilely prepared by thermal treatment. The optimized photocatalyst (CNF_{100}) first showed excellent photoactivity for killing a variety of bacteria (93.0% for *E. coli*, 93.9% for *Salmonella*, and 96.2% for *S. aureus*) under visible light irradiation. The superior activity can be attributed to the formation of shallow electron traps (Fe−N_3) that can capture excitons of excited states, which promote the charge transfer and energy transfer process of activated adsorbed molecular oxygen, respectively, forming reactive oxygen species, improving separation efficiency of photoexcited electrons and holes, and the Fe−N_3 traps can also be used as photosensitive sites to broaden the absorption range of visible light. This strategy of constructing shallow electronic traps lays a theoretical foundation for the design of new environmentally friendly and efficient water disinfectants.

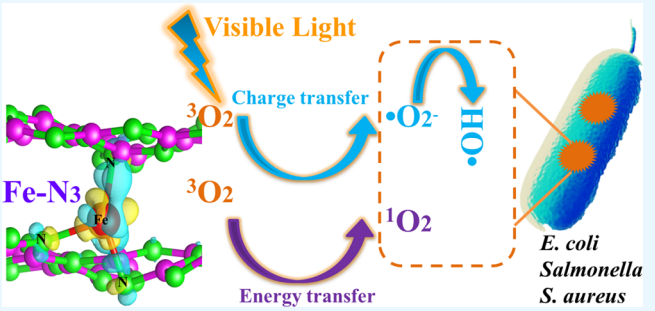

INTRODUCTION

Effectively reducing the bacterial colony number in water is crucial to solve the global public health problem.[1−4] Excessive bacteria in drinking water can induce infectious diseases such as bacillary dysentery and hepatitis A virus, threatening human life.[5,6] For example, diarrhea caused by drinking contaminated water infect hundreds of millions of people and kill about two million children each year in the world.[7−9] Often used water sterilization methods mainly include chlorination, ultraviolet and ozone disinfection, etc.[2,3,10,11] However, the toxic byproducts generated during the disinfection process increase the risk of cancer, and the operation is complicated and expensive.[12,13] Therefore, there is an urgent need to develop a novel antibacterial technology with high efficiency, low cost, and universal application.

Among various antibacterial technologies, photocatalytic disinfection, as a green and sustainable strategy,[14−17] has been widely promoted due to its rapid and efficient inactivation effect without obvious drug resistance and side effects, and the antibacterial process driven by solar energy is controllable, recyclable, and has a low cost.[18−20] As an exogenous antibacterial technology, it relies on induced generation of reactive oxygen radicals (superoxide radicals, hydroxyl radicals, etc.) to cause bacterial inactivation without chemical additives or harmful inactivation byproducts.[21,22] Therefore, we believe that the design of environmentally friendly and efficient semiconductor sterilization materials show broad application prospects, especially in water disinfection.

Graphite carbon nitride (g-C_3N_4), as a common semiconductor fungicide, has attracted great attention owing to its terrific biocompatibility and stability.[20,23,24] However, it has some shortcomings that limit application, such as high carrier recombination and a narrow visible light response range (400−450 nm).[25−27] Modification of transition metals has been recognized as an important strategy that can significantly improve the photocatalytic performance of g-C_3N_4.[12,28,29] Cu, Mn, or Co atoms anchoring could greatly increase the in-plane and interlayer carrier separation and transfer of g-C_3N_4, thereby improving the photocatalytic efficiency, which in turn exhibits excellent photocatalytic performance.[28−30] These statements confirm the fact that by introducing transition metals into g-C_3N_4, the charge transfer process has been closely studied to activate molecular oxygen to form highly oxidizing superoxide radicals under photoexcitation, but the accompanying energy transfer process to generate singlet oxygen has rarely been analyzed in detail, which makes it difficult to clarify the actual photocatalytic bactericidal mechanism. To be sure, g-C_3N_4 is considered to be a strong exciton material with low dielectric properties, and its exciton

Received: April 18, 2023
Accepted: July 5, 2023
Published: July 22, 2023

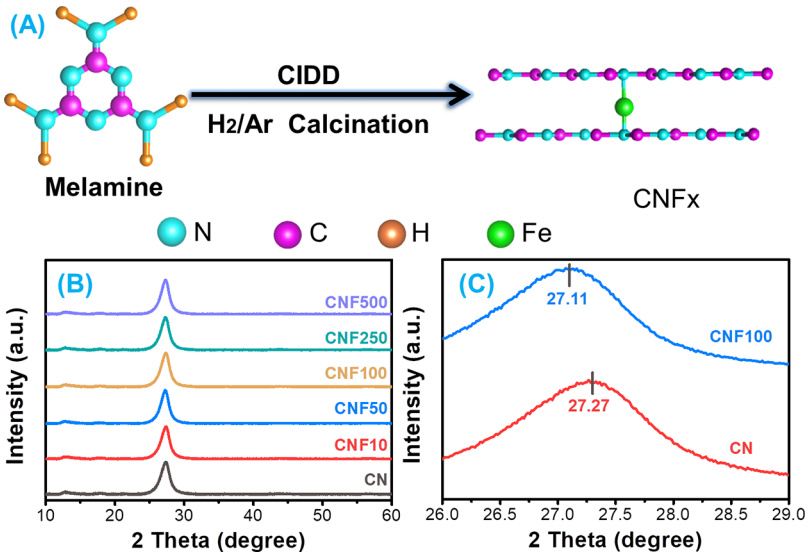

Figure 1. Schematic illustration of the as-prepared CNF*x* samples (A), XRD patterns (B), and corresponding close comparison (C).

binding energy (evaluation of exciton strength important index) is assumed to be extremely high, much greater than some typical inorganic semiconductors.[23,31] As mentioned above, the huge Coulomb interaction between photoexcited electron−hole pairs in g-C_3N_4 prevents the dissociation of excitons and charge carriers, thus inhibiting the charge transfer efficiency.[23,32] Although the conspicuous influence of excitons reduces the charge transfer efficiency, it may touch some pivotal process of energy transfer under illumination, such as the molecular oxygen in the ground state is activated by high-energy excitons into singlet oxygen in the spin triplet state.[23,33] Inspired by the above, the g-C_3N_4 catalyst modified by transition metals was developed, which can not only significantly improve the charge transfer of excitons but also enhance the energy transfer of charge carriers, activating molecular oxygen to generate a variety of active species. For some reactions, such as water disinfection, that require a number of free reactive oxygen species as the main antibacterial active substance, it should be predicted that using this type of disinfectant will show great potential and advantage under aerobic conditions.

In this work, we reported that dispersed Fe atoms were successfully inserted into g-C_3N_4 by a simple pyrolysis strategy under a reducing atmosphere. The introduction of Fe atoms could form Fe−N_3 shallow charge trapping centers between the layers of g-C_3N_4, which copromote the energy transfer and charge transfer process of high-energy excitons, improve the separation of charge carriers, accelerate the process of molecular oxygen conversion to superoxide radicals and singlet oxygen, and also broaden the response range of visible light. Therefore, the preferred catalyst, CNF_{100}, exhibited highly effective and universal inhibition against *E. coli*, *Salmonella*, and *S. aureus*. This provides a new idea to develop a safe and green water disinfectant with superior sterilization.

EXPERIMENTAL PROCEDURES

Preparation of CNF*x* photocatalysts: Typically, 100 mg of the cyclopentadienyl iron(II) dicarbonyl dimer (CIDD) was ultrasonically dissolved in 250 mL of *N*,*N*-dimethylformamide, and 10.0 g of melamine was added to the above solution under magnetic stirring for 12 h. After filtering and rotary evaporation, the red brown solid was kept for overnight vacuum drying under 70 °C and then transferred into a tube furnace at 550 °C for 4 h in H_2/Ar (10%/90% vol) with a heating rate of 1 °C/min, resulting the CNF_{100} sample, where "100" in the subscript of CNF_{100} was representative of the added mass of the CIDD. For comparison, when no CIDD was added, the sample being prepared was labeled as CN under the same conditions. Please note that the details of catalyst characterization, photoelectrochemical measurement, photocatalytic antibacterial tests, live/dead staining, and the calculation of DFT are presented in the Supporting Information.

RESULTS AND DISCUSSION

The schematic of the prepared CNF*x* (Fe−N_3 sites modified g-C_3N_4) with inexpensive methods is presented in Figure 1A. CNF*x* were synthesized via a thermal method at 550 °C for 4 h in a reducing atmosphere using CIDD as the Fe source and melamine to get the CNF*x* catalysts. XRD patterns of the CN sample showed two main peaks at 13.1 and 27.2°, which appeared from the (100) and (002) planes of g-C_3N_4, as shown in Figure 1B,[12,34] and no XRD peaks of oxides and elemental of iron are observed in Figure 1B. Astoundingly, the XRD diffraction angle decreased from 27.27 on the CN sample to 27.11 on the CNF_{100} sample, which might explain the increase of the interlayer distance by introducing Fe into the g-C_3N_4 interlayer.[35,36] In addition, as shown in Figure S1, the vibration peaks were observed at 1650−1250 cm^{-1}, matching with the heterocycles of g-C_3N_4,[23,28] and no absorption peaks of the CIDD and Fe species were seen in FT-IR spectra (Figure S1), reflecting that Fe species were evenly dispersed in g-C_3N_4, which matched with XRD results. From theoretical calculation's standpoint, when Fe atoms were embedded between layers of g-C_3N_4, the interlayer distance increased from 3.2 Å over the optimized g-C_3N_4 moder (gCN) to 3.5 Å over g-C_3N_4 moder modified by Fe atoms (CNFe), as shown in Figure S2. These results indicated that the Fe atoms were successfully embedded in the interlayer of g-C_3N_4 by a simple strategy of thermal cleavage of Fe-containing organic ligands.

In addition, the morphology of all the as-prepared samples were characterized by SEM and TEM. CN and CNF_{100}

https://doi.org/10.1021/acsomega.3c02654
ACS Omega 2023, 8, 27276−27283

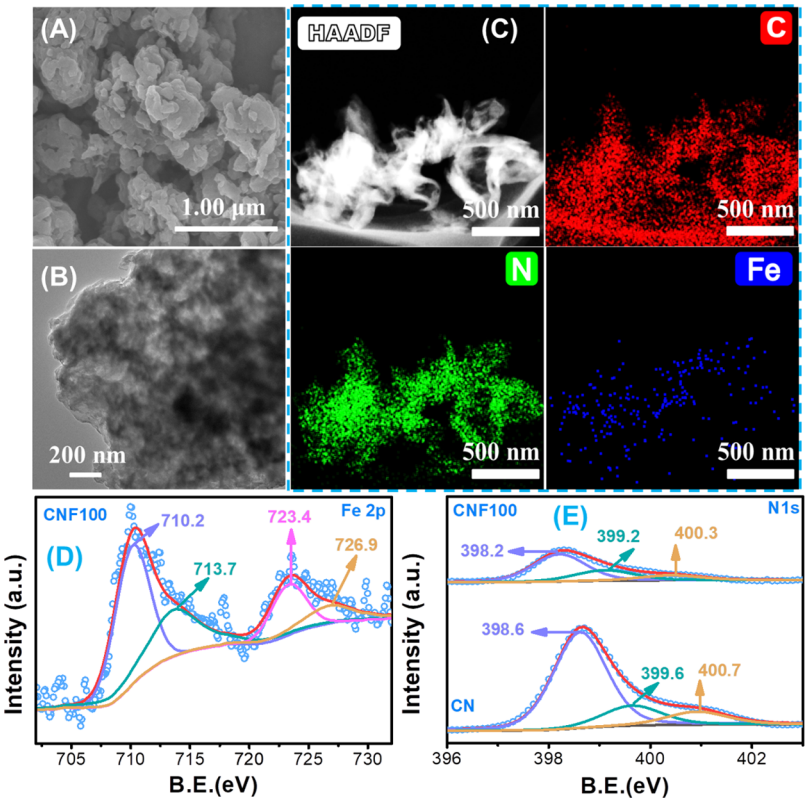

Figure 2. SEM (A), TEM (B), and EDX mapping (C) of the CNF_{100} photocatalyst. XPS Fe 2p (D) and N 1s (E) spectra.

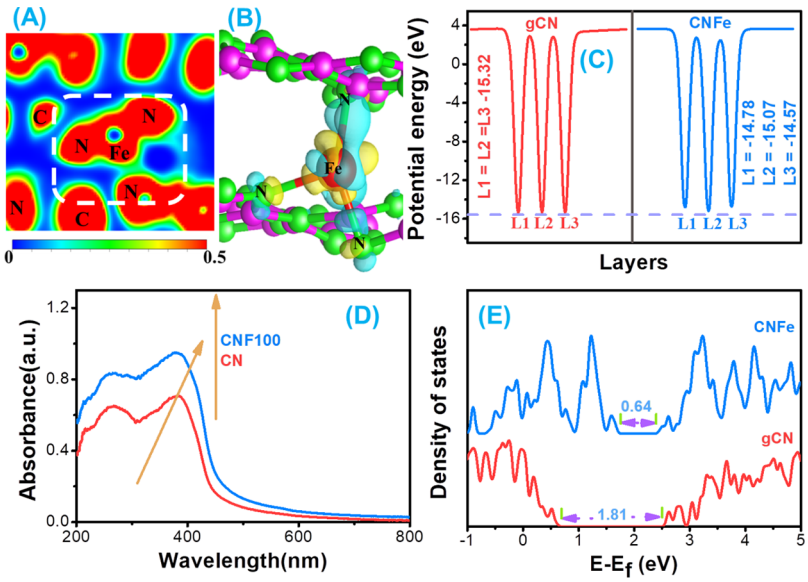

Figure 3. Electron local function (A), charge difference distribution (B), and electrostatic potential (C) for the calculated CNFe, where the blue and yellow electron cloud denoted the accumulated charge and depleted charge, respectively. DRS spectra (D) and density of states (E).

samples were composed of a 2D-layered g-C_3N_4, as shown in Figures 2A and S3, predicting that the insertion of Fe atoms did not destroy the layered structure of g-C_3N_4. As illustrated in Figure 2B, the microstructure of the CNF_{100} sample consisted of multiple layers of g-C_3N_4. The distribution of C, N, and Fe elements were completely concentrated on the g-C_3N_4 sheet by element mapping (Figure 2C), respectively. Note that agglomerated Fe atoms were not observed, reconfirming that Fe was uniformly embedded in g-C_3N_4 as highly dispersed atoms, rather than elemental and corresponding oxides. Moreover, the chemical states of N and Fe elements for the prepared samples were further investigated by XPS analysis. The high-resolution N 1s spectra of CNF_{100} samples are shown in Figure 2D. It could be seen that four fitted peaks of CNF100 samples were located in Fe $2p_{3/2}$ and $2p_{1/2}$ peaks at 713.7, 726.9 eV over Fe^{3+} and 710.2, 723.4 eV over Fe^{2+}, respectively (Figure 2D).[37,38] The three simulated peaks of N 1s spectra for the CN sample were observed at 398.6, 399.6, and 400.7 eV, corresponding to C=N−C, N−$(C)_3$, and N−H groups in g-C_3N_4,[25,39] respectively (Figure 2E). Equally, the

https://doi.org/10.1021/acsomega.3c02654
ACS Omega 2023, 8, 27276−27283

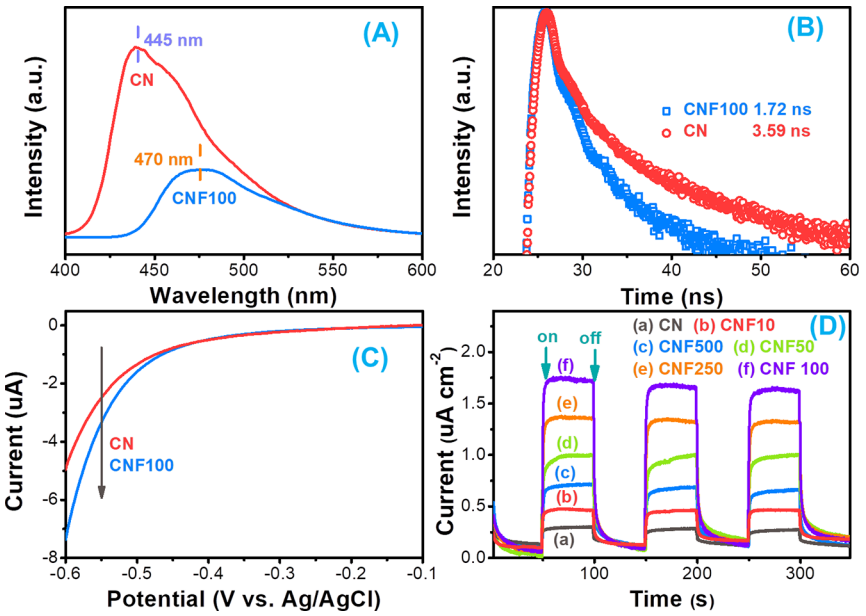

Figure 4. Photoluminescence spectra (A), time-resolved transient fluorescence decay (B), cathodic polarization curves (C), and photocurrent (D).

CNF_{100} sample N 1s spectrum was successfully fitted by the above three peaks, suggesting that the structure of g-C_3N_4 was still retained in CNF_{100}. It should be noted that the binding energy of the N 1s peak for CNF_{100} was reduced to 0.4 eV with comparison of the CN sample because of the interaction of Fe−N_x bonding. Furthermore, the atomic ratio of the Fe element in CNF_{250} was estimated to be 3.72% by XPS analysis (Table S1).

The driving forces causing the interaction of Fe and N atoms were deliberated by means of DFT calculations. When the Fe atoms was inserted into the structure of g-C_3N_4, the corresponding electron local function is shown in Figure 3A. As can be seen in Figure 3A, the Fe atoms appeared to overlap with the electron clouds of one N atom in the first layer and two N atoms in the second layer in g-C_3N_4 (white dotted box), which indicated the formation of Fe−N_3 sites between layers of g-C_3N_4. Similarly, differential charge distribution, as shown in Figure 3B, was found to reduce electron cloud density for the Fe atoms, but the corresponding change of N atoms was contrary to this, confirming the obvious charge transfer between one Fe atom and three N atoms. In addition, Fe−N_3 sites around the blue electron cloud was greater than the yellow electron cloud, which further showed that these sites induced shallow electron trapping (Figure 3B)[31] and then promoted the charge transfer, which in turn embodied superior separation efficiency of photoexcited carriers. Moreover, the electrostatic potential of the three layers in the CNFe model (L1 = 14.78 eV, L2 = 15.07 eV, and L3 = 14.57 eV) was smaller than that of gCN (L1 = L2 = L3 = 15.32 eV), as shown in Figure 3C, which meant that CNFe was endowed with a lower energy barrier than gCN to achieve rapid charge transfer in the Z-direction as a result of the existence of the shallow electron trap of Fe−N_3.

The optical capture capability, as the factors to improve the photocatalytic activity, was obtained by admeasuring the diffuse reflectance spectroscopy (DRS) of the sample in the 200−800 nm range (Figure 3D).[12,25] As exhibited in Figure 3D, the light absorption for CN (λ < 450 nm) was attributed to the intrinsic response of the band gap, and the as-prepared CNF_{100} demonstrated an increased light capture efficiency in the visible region relative to CN, especially from 400 to 600 nm. Similarly, the DFT theoretical used to calculate the total density of states (TDOS) was endowed with the homologous tendency. TDOS is shown in Figure 3E, and the band gap of CNFe and gCN was identified to be 0.64 and 1.81 eV, respectively, with mismatching experiment consequence owing to limitations of DFT theoretical.[36] These facts suggested the increased capture ability of visible light for g-C_3N_4 due to the introduction of the Fe−N_3 site.

Additionally, the separation degree of photoexcited electron−hole pairs, as one of the basic drivers of the enhancing photocatalytic activity, was studied through the characterization of photoelectric properties. As displayed in Figure 4A, the PL intensity of the CNF_{100} sample was lower than that of CN, meaning that the introduced Fe sites could refrain expressively the radiated recombination of carriers. Surprisingly, the maximum wavelength of fluorescence emission redshifts from 445 to 470 nm with the insertion of Fe atoms into the interlayer of g-C_3N_4 (Figure 4A), suggesting that the excited charges transferred to the surface of the catalyst, accompanied by energy transfer during the photoexcited carrier separation process on account of the existence of shallow electron traps.[40] According to time-resolved fluorescence decay spectroscopy (TRFDS) in Figure 4B, the average lifetime ($\tau_{average}$ = 1.72 ns) of the CNF_{100} sample was reduced compared with those of CN ($\tau_{average}$ = 3.59 ns), signifying that the short singlet exciton lifetime could enhance the dissociation of the exciton at the Fe−N_3 sites to facilitate the energy transfer process,[41] increasing in the transition rate of the electron from the excited state to the ground state[26,41] and improving the catalytic performance. Meanwhile, linear sweep voltammetry (LSV) measurements could provide further insight into the separation efficiency of photoexcited electron−hole pairs. As shown in Figure 4C, the current at the threshold potential of CNF_{100} was significantly stronger than that of CN, and the photocurrent of CNF_{100} and all Fe−N_3-modified samples (CNFx) was higher than that of CN (0.3 μA × cm^{-2}) at illumination, as seen from Figure 4D, especially for

https://doi.org/10.1021/acsomega.3c02654
ACS Omega 2023, 8, 27276−27283

the CNF_{100} sample with the maximum current at 1.2 $\mu A \times cm^{-2}$, also proving the stronger separation performance of electron−hole pairs. Moreover, the photocurrent decreased from 1.2 $\mu A \times cm^{-2}$ for CNF_{100} to 0.6 for CNF_{500}, and it may be caused by excessive shallow traps that aggravated the recombination of photoexcited carriers.

The superior photocatalytic performance of CNF*x* to g-C_3N_4 was evaluated by the sterilization of *E. coli* and a schematic of the corresponding antibacterial device is shown in Figure S4. CNF_{100} was used as the representative CNF*x* catalyst to compare with g-C_3N_4, as it showed the best performance as stated in the above characterizations. According to the results of the blank experiment (Figure 5A,B,O), there was no change in the colonies of *E. coli* before

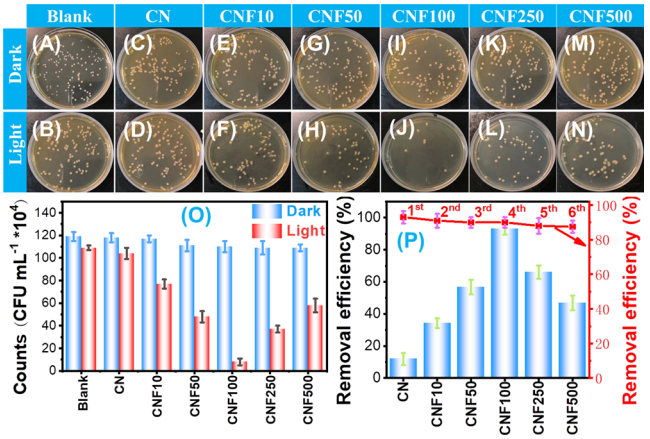

Figure 5. *E. coli* colony images of blank (A, B) and as-prepared samples (C−N) before and after illumination, statistics on the counts of colonies (O), and sterilization rate and cycle test (P).

(1.19 CFU $mL^{-1} \times 10^6$) and after (1.09 CFU $mL^{-1} \times 10^6$) illumination without the photocatalyst, which not only indicated that the lighting condition did not result in the reproduction of *E. coli* but also confirmed that the process of killing *E. coli* was driven by visible light. As shown in Figure 5C,D,O, when introducing CN as the catalyst, the colony count decreased from 1.18 CFU $mL^{-1} \times 10^6$ under dark to 1.04 CFU $mL^{-1} \times 10^6$ under illumination (Figure 5C,D,O) and the sterilization of *E. coli* proceeded sluggishly over CN with a low conversion of 11.8% (Figure 5P), respectively. In accordance with the characterization data, the sterilizing rate of *E. coli* first increased with an increase of the Fe content on g-C_3N_4 and then decreased (Figure 5E−O). To our delight, CNF_{100} was the best photocatalyst for this killing process, and *E. coli* was killed in a high efficiency of 93.0% after 30 min, as shown in Figure 5P (the number of corresponding colonies reduced from 1.10 CFU $mL^{-1} \times 10^6$ to 0.08 CFU $mL^{-1} \times 10^6$ in Figure 5O). To our expectation, the representative catalyst (CNF_{100}) was 7.8 times more efficient in sterilization than the original g-C_3N_4. With the increase of Fe content, we observed that the bactericidal efficiency of CNF_{250} and CNF_{500} decreased from 93.0 to 66 and 47% (Figure 5P), respectively, which might be caused by the excessive Fe atoms forming carrier recombination sites in the catalyst and then promoting the recombination of photoexcited carriers, which was consistent with the results of photocurrent. Moreover, CNF_{100} still maintained superior removal efficiency of *E. coli* after a six cycle test (red line, Figure 5P) and no obvious changes of the XRD peak were observed before and after sterilization (Figure S5), indicating that the optimized catalyst exhibited great stability.[42] The excellent antibacterial effect of the as-prepared catalysts was further investigated by other methods. The fluorescent dye mapping images are shown in Figure 6A,B for before and after sterilization, respectively, and

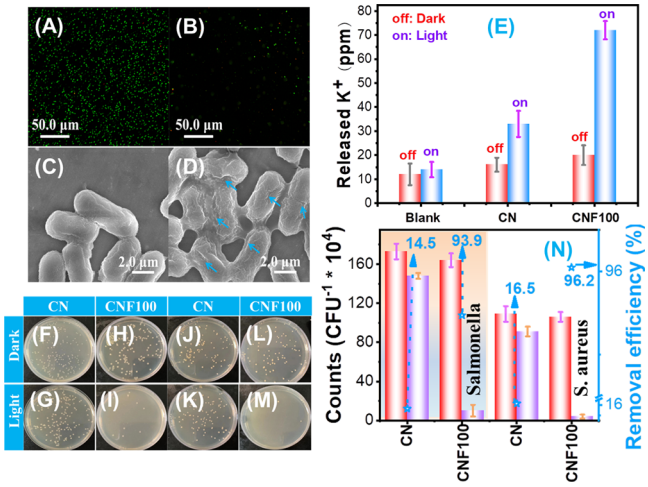

Figure 6. Fluorescent dye mapping images of before (A) and after (B) irradiation by CNF_{100}, SEM images under the dark (C) and light (D) by CNF_{100}, the concentration of K^+ leakage of *E. coli* cells (E), the colony images of *Salmonella* (F−I) and *S. aureus* (J−M) before and after illumination, statistics on the counts of *Salmonella* and *S. aureus* colonies and the corresponding sterilization rate (N).

the green and red dots denoted the living and dead cells, respectively. It can be clearly observed that the number of living *E. coli* cells was significantly less than that of without CNF_{100} as a disinfectant. Needs to show that, the little red spot was observed in Figure 6B, this possibility was ultra ascendant sterilization activity, leading to cellular structure was completely destroyed. Moreover, fresh *E. coli* showed smooth cell membranes and cell walls (Figure 6C), while after 30 min of visible light irradiation, many folds and breakage were found, as shown in Figure 6D, on account of the destruction of the cell membrane and cell wall. After all, as is known, K^+ diffuses outside the cell, as the cell membrane and cell wall break down.[12] The K^+ concentration of CNF_{100} rapidly increased to about 70 ppm with the comparation of CN (33 ppm) after irradiation under visible light for 30 min (Figure 6E). These results reconfirmed the fact that CNF*x* could destroy the cell structure, exhibiting the high photocatalytic killing efficiency.

In order to better reflect the optimized catalyst as a potentially useful disinfectant in the water treatment process, the other bacteria (*Salmonella* and *S. aureus*) were further used as targets to evaluate its satisfactory performance. The colony images of *Salmonella* and *S. aureus* before and after sterilization are shown in Figure 6F−M and the corresponding number of colonies is recorded in Figure 6N. Compared with CN (14.5%), the *Salmonella* sterilization rate of CNF_{100} (93.9%) is significantly greater in Figure 6N. Similarly, the killing rate of *S. aureus* also increased from 16.5% for CN to 96.2% for CNF_{100} after irradiation for 30 min (Figure 6N). Based on these, it can be determined that g-C_3N_4 catalysts with Fe−N_3 sites have excellent universality, indicating that they are considered to have broad application in water disinfection.

https://doi.org/10.1021/acsomega.3c02654
ACS Omega 2023, 8, 27276−27283

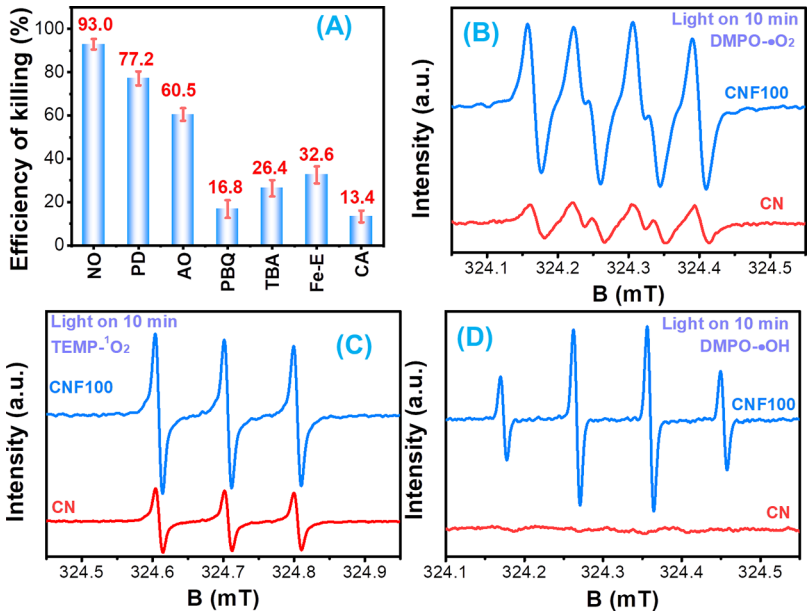

Figure 7. Photocatalytic inactivation of *E. coli* by CNF_{100} with scavengers (A) under illumination. PD, AO, PBQ, TBA, Fe−E, and CA could quench e^-, h^+, $^{\cdot}O_2^-$, $^{\cdot}OH$, H_2O_2, and $^1O_2$. "NO" indicated that no scavengers were added, respectively. The ESR signal of trapped $^{\cdot}O_2^-$ (B), $^1O_2$ (C), and $^{\cdot}OH$ (D).

The bactericidal mechanism in the aerobic system mainly depends on the superoxidizing ability of reactive oxygen species.[12,13,43] When e^- and h^+ were quenched using potassium dichromate (PD) and ammonium oxalate (AO), the corresponding *E. coli* inactivation rate decreased from 93 to 77.2 and 60.5%, respectively (Figure 7A). In particular, the corresponding *E. coli* killing rate dropped obviously to 16.8, 26.4, 32.6, and 13.4% with the scavengers of $^{\cdot}O_2^-$ (*P*-benzoquinone, PBQ), $^{\cdot}OH$ (*tert*-butanol, TBA), H_2O_2 (Fe-EDTA, Fe−E), and $^1O_2$ (*β*-carotene, CA), respectively (Figure 7A). This indicated that CNF*x* photocatalysts relied on $^{\cdot}O_2^-$, $^{\cdot}OH$, H_2O_2, and $^1O_2$, as the major active species during photocatalytic inactivation, instead of e^- and h^+. Here, it is needed to be stated that the generation of $^{\cdot}O_2^-$ and $^1O_2$ originated from the charge transfer and energy transfer process between the exciton and adsorbed O_2 in the ground state, respectively.[33] Furthermore, the electron spin resonance signal (ESR) of the $^{\cdot}O_2^-$, $^1O_2$, and $^{\cdot}OH$ adducts of CNF_{100} was stronger than that of CN under illumination (Figure 7B−D). Curiously, the generation of $^{\cdot}OH$ in g-C_3N_4 was restricted by activation of water due to the thermodynamic challenge, whereas it was detected in this system, possibly because it can be converted to $^{\cdot}OH$ via $^{\cdot}O_2^-$ using H_2O_2 as an intermediate.[36,44]

On considering that BET surface area of the photocatalyst plays an important role in its photoreactivity, we measured the nitrogen sorption isotherms of the photocatalysts. Figure S6A,B compares the nitrogen sorption isotherms and corresponding pore size distribution curves of the photocatalysts. Since the BET surface areas, pore volume, and average pore size of all samples are similar (Table S2), the introduction of Fe atoms did not affect the textural properties of g-C_3N_4 and the enhanced photoreactivity should be attributed to the introduction of Fe−N_3 sites instead of the BET surface area. According to these elaborations, a possible mechanism of photocatalytic killing of bacteria was proposed as follows: Fe−N_3 sites in g-C_3N_4, as shallow electron traps, captured the first excited state of charges through the electron transfer and energy transfer process to activate molecular oxygen and form $^{\cdot}O_2^-$ and $^1O_2$, respectively, and then $^{\cdot}O_2^-$ was further transformed into $^{\cdot}OH$ by the intermediate of H_2O_2. Finally, these species with strong oxidizing ability destroyed the cell membrane and cell wall of bacteria, resulting in their death.

CONCLUSIONS

In summary, Fe atoms were inserted into g-C_3N_4 layers to form the Fe−N_3 sites by the simple thermal treatment method with superior activity of the universality of killing bacteria under illumination. A series of characterization in combination with DFT theoretical calculation revealed that the sites can not only be used as a shallow electron trap to efficiently capture excitons into strongly oxidizing reactive oxygen species through activation of molecular oxygen with energy and charge transfer but also enhance the ability to capture light as well, especially under visible light, leading to the optimized photocatalyst (CNF_{100}) showing excellent performance of killing many types of bacteria. This study provides a novel research idea for establishing shallow electron traps on the surface of photocatalysts, which would be conducive to the development of more universal and excellent semiconductor sterilization materials in the future.

ASSOCIATED CONTENT

Supporting Information

The Supporting Information is available free of charge at https://pubs.acs.org/doi/10.1021/acsomega.3c02654.

The characterization, photoelectrochemical measurement, photocatalytic antibacterial tests, live/dead staining, DFT calculations, FT-IR spectra, optimized structure, SEM image, schematic diagram, nitrogen adsorption−desorption isotherms, and the corresponding pore size distribution curves (PDF)

https://doi.org/10.1021/acsomega.3c02654
ACS Omega 2023, 8, 27276−27283

AUTHOR INFORMATION

Corresponding Authors

Zhao Hu − *National Key Laboratory of Green Pesticide, Key Laboratory of Green Pesticide & Agricultural Bioengineering, Ministry of Education, State-Local Joint Laboratory for Comprehensive Utilization of Biomass, Center for R&D of Fine Chemicals, Guizhou University, Guiyang, Guizhou 550025, China*; orcid.org/0000-0001-5526-3826; Email: gs.zhu21@gzu.edu.cn

Yujiao Zhang − *Institute of Animal Husbandry and Veterinary Medicine, Guizhou Academy of Agricultural Sciences, Guiyang 550005, China; National Key Laboratory of Green Pesticide, Key Laboratory of Green Pesticide & Agricultural Bioengineering, Ministry of Education, State-Local Joint Laboratory for Comprehensive Utilization of Biomass, Center for R&D of Fine Chemicals, Guizhou University, Guiyang, Guizhou 550025, China*; Email: gs.yxzhang21@gzu.edu.cn

Authors

Ling Pu − *Institute of Animal Husbandry and Veterinary Medicine, Guizhou Academy of Agricultural Sciences, Guiyang 550005, China*

Jiying Wang − *College of Animal Science and Technology, Huaihua Polytechnic College, Huaihua 418000, China; College of Veterinary Medicine, Hunan Agricultural University, Changsha 410000, China*

Complete contact information is available at: https://pubs.acs.org/10.1021/acsomega.3c02654

Author Contributions

L.P., J.W., Y.Z., and Z.H. proposed the ideas, analyzed the data, wrote the manuscript, and discussed in this work. Y.Z. supported the DFT calculations.

Notes

The authors declare no competing financial interest.

ACKNOWLEDGMENTS

The authors thank the Guizhou Province Science and Technology Plan Project (Grant No. QKH [2020]1Y042) and the Graduate Research Foundation of Guizhou Province (YJSKYJJ [2021] 039, YJSKYJJ [2021] 040).

REFERENCES

(1) Mitcheltree, M. J.; Pisipati, A.; Syroegin, E. A.; Silvestre, K. J.; Klepacki, D.; Mason, J. D.; Terwilliger, D. W.; Testolin, G.; Pote, A. R.; Wu, K. J. Y.; Ladley, R. P.; Chatman, K.; Mankin, A. S.; Polikanov, Y. S.; Myers, A. G. A synthetic antibiotic class overcoming bacterial multidrug resistance. *Nature* **2021**, *599*, 507−512.

(2) Sadowska, J. M.; Genoud, K. J.; Kelly, D. J.; O'Brien, F. J. Bone biomaterials for overcoming antimicrobial resistance: Advances in nonantibiotic antimicrobial approaches for regeneration of infected osseous tissue. *Mater. Today* **2021**, *46*, 136−154.

(3) Li, R.; Chen, T. T.; Pan, X. L. Metal-organic-framework-based materials for antimicrobial applications. *ACS Nano* **2021**, *15*, 3808−3848.

(4) Wang, H.; Wu, Y.; Feng, M.; Tu, W.; Xiao, T.; Xiong, T.; Ang, H.; Yuan, X.; Chew, J. W. Visible-light-driven removal of tetracycline antibiotics and reclamation of hydrogen energy from natural water matrices and wastewater by polymeric carbon nitride foam. *Water Res.* **2018**, *144*, 215−225.

(5) Du, M. R.; Zhao, W. B.; Ma, R. N.; Xu, H.; Zhu, Y. P.; Shan, C. X.; Liu, K. K.; Zhuang, J.; Jiao, Z. Visible-light-driven photocatalytic inactivation of *S.* aureus in aqueous environment by hydrophilic zinc oxide (ZnO) nanoparticles based on the interfacial electron transfer in *S.* aureus/ZnO composites. *J. Hazard. Mater.* **2021**, *418*, No. 126013.

(6) Unemo, M.; Jensen, J. S. Antimicrobial-resistant sexually transmitted infections: gonorrhoea and mycoplasma genitalium. *Nat. Rev. Urol.* **2017**, *14*, 139−152.

(7) Amábile-Cuevas, C. Society must seize control of the antibiotics crisis. *Nature* **2016**, *533*, 439−439.

(8) Heymann, D. L. Resistance to anti-infective drugs and the threat to public health. *Cell* **2006**, *124*, 671−675.

(9) Farha, M. A.; French, S.; Brown, E. D. Systems-level chemical biology to accelerate antibiotic drug discovery. *Acc. Chem. Res.* **2021**, *54*, 1909−1920.

(10) Li, G. Y.; Nie, X.; Chen, J. Y.; Jiang, Q.; An, T. C.; Wong, P. K.; Zhang, H. M.; Zhao, H. J.; Yamashita, H. Enhanced visible-light-driven photocatalytic inactivation of Escherichia coli using g-C_3N_4/TiO_2 hybrid photocatalyst synthesized using a hydrothermal-calcination approach. *Water Res.* **2015**, *86*, 17−24.

(11) Zhang, R. M.; Song, C. J.; Kou, M. P.; Yin, P. Q.; Jin, X. L.; Wang, L.; Deng, Y.; Wang, B.; Xia, D. H.; Wong, P. K.; Ye, L. Q. Sterilization of escherichia coli by photothermal synergy of WO_3-x/C nanosheet under infrared light irradiation. *Environ. Sci. Technol.* **2020**, *54*, 3691−3701.

(12) Hu, Z.; Zhang, Y. J.; Pu, L.; Wang, B. Y.; Yang, S.; Li, H. Atomic Ti-Nx sites with switchable coordination number for enhanced visible-light photocatalytic water disinfection. *J. Cleaner Prod.* **2022**, *377*, No. 134423.

(13) Xia, P. F.; Cao, S. W.; Zhu, B. C.; Liu, M. J.; Shi, M. S.; Yu, J. G.; Zhang, Y. F. Designing a 0D/2D s-scheme heterojunction over polymeric carbon nitride for visible-light photocatalytic inactivation of bacteria. *Angew. Chem., Int. Ed.* **2020**, *59*, 5218−5225.

(14) Akhundi, A.; Badiei, A.; Ziarani, G. M.; Habibi-Yangjeh, A.; Muñoz-Batista, M. J.; Luque, R. Graphitic carbon nitride-based photocatalysts: Toward efficient organic transformation for value-added chemicals production. *Mol. Catal.* **2020**, *488*, No. 110902.

(15) Sabri, M.; Habibi-Yangjeh, A.; Rahim Pouran, S.; Wang, C. D. Titania-activated persulfate for environmental remediation: the-state-of-the-art. *Catal. Rev.* **2023**, *65*, 118−173.

(16) Feizpoor, S.; Rahim Pouran, S.; Habibi-Yangjeh, A. Recent progress on photocatalytic evolution of hydrogen gas over TiO_2-x-based emerging nanostructures. *Mater. Sci. Semicond. Process.* **2023**, *162*, No. 107444.

(17) Wang, H.; Yang, Y.; Yuan, X. Z.; Liang Teo, W.; Wu, Y.; Tang, L.; Zhao, Y. L. Structure−performance correlation guided applications of covalent organic frameworks. *Mater. Today* **2022**, *53*, 106−133.

(18) Liu, Z. L.; Gao, W. Z.; Liu, L. Z.; Luo, S. J.; Zhang, C.; Yue, T. L.; Sun, J.; Zhu, M. Q.; Wang, J. L. Work function mediated interface charge kinetics for boosting photocatalytic water sterilization. *J. Hazard. Mater.* **2023**, *442*, No. 130036.

(19) Lian, Q. Y.; Liang, Z. C.; Guan, X. Y.; Tang, Z. Y.; Zhang, R. M.; Yang, B. Y.; Wu, Y. X.; Zhao, H. N.; He, C.; Xia, D. H. High-coordinated BiV/BiIV regulates photocatalytic selective activation of structural oxygen and self-generated H_2O_2 dominating an efficient synergistic sterilization. *Appl. Catal. B* **2023**, *331*, No. 122724.

(20) Zhang, X.; Tian, F. Y.; Lan, X.; Liu, Y. Q.; Yang, W. W.; Zhang, J.; Yu, Y. S. Building P-doped MoS_2/g-C_3N_4 layered heterojunction with a dual-internal electric field for efficient photocatalytic sterilization. *Chem. Eng. J.* **2022**, *429*, No. 132588.

(21) Ma, C. C.; Wang, W.; Li, W.; Sun, T. X.; Feng, H. M.; Lv, G. J.; Chen, S. G. Full solar spectrum-driven Cu_2O/PDINH heterostructure with enhanced photocatalytic antibacterial activity and mechanism insight. *J. Hazard. Mater.* **2023**, *448*, No. 130851.

(22) Jin, C.; Sun, D. N.; Sun, Z. T.; Rao, S. S.; Wu, Z. R.; Cheng, C.; Liu, L.; Liu, Q. Q.; Yang, J. Interfacial engineering of Ni-phytate and Ti_3C_2Tx MXene-sensitized TiO_2 toward enhanced sterilization efficacy under 808 nm NIR light irradiation. *Appl. Catal. B* **2023**, *330*, No. 122613.

(23) Zhang, G. Q.; Xu, Y. S.; Rauf, M.; Zhu, J. Y.; Li, Y. L.; He, C. X.; Ren, X. Z.; Zhang, P. X.; Mi, H. W. Breaking the Limitation of Elevated Coulomb Interaction in Crystalline Carbon Nitride for

Visible and Near-Infrared Light Photoactivity. *Adv. Sci.* **2022**, *9*, No. 2201677.
(24) Akhundi, A.; Zaker Moshfegh, A.; Habibi-Yangjeh, A.; Sillanpä, M. Simultaneous dual-functional photocatalysis by g-C_3N_4-based nanostructures. *ACS EST Eng.* **2022**, *2*, 564−585.
(25) Wang, B. Y.; Guo, X. D.; Zhang, Y. J.; Wang, Y.; Huang, G. Q.; Chao, H. X.; Wang, W. J.; Hu, Z.; Yan, X. M. Extraordinary promotion of visible-light hydrogen evolution for graphitic carbon nitride by introduction of accumulated electron sites (BN_2). *ACS Appl. Energy Mater.* **2022**, *5*, 7479−7489.
(26) Zhao, D. M.; Wang, Y. Q.; Dong, C. L.; Huang, Y. C.; Chen, J.; Xue, F.; Shen, S. H.; Guo, L. J. Boron-doped nitrogen-deficient carbon nitride-based Z-scheme heterostructures for photocatalytic overall water splitting. *Nat. Energy* **2021**, *6*, 388−397.
(27) Dai, Y. T.; Li, C.; Shen, Y. B.; Lim, T. B.; Xu, J.; Li, Y. W.; Niemantsverdriet, H.; Besenbacher, F.; Lock, N.; Su, R. Light-tuned selective photosynthesis of azo- and azoxy-aromatics using graphitic C_3N_4. *Nat. Commun.* **2018**, *9*, 60.
(28) Xiao, X.; Gao, Y.; Zhang, L.; Zhang, J.; Zhang, Q.; Li, Q.; Bao, H.; Zhou, J.; Miao, S.; Chen, N.; Wang, J.; Jiang, B.; Tian, C.; Fu, H. A promoted charge separation/transfer system from Cu single atoms and C_3N_4 layers for efficient photocatalysis. *Adv. Mater.* **2020**, *32*, No. 2003082.
(29) Chen, Z.; Zhao, J. X.; Cabrera, C. R.; Chen, Z. F. Computational screening of efficient single-atom catalysts based on graphitic carbon nitride (g-C_3N_4) for nitrogen electroreduction. *Small. Methods* **2019**, *6*, No. 1800368.
(30) Guo, Z.; Xie, Y. B.; Xiao, J. D.; Zhao, Z. J.; Wang, Y. X.; Xu, Z. M.; Zhang, Y.; Yin, L. C.; Cao, H. B.; Gong, J. L. Single-atom Mn-N_4 site-catalyzed peroxone reaction for the efficient production of hydroxyl radicals in an acidic solution. *J. Am. Chem. Soc.* **2019**, *141*, 12005−12010.
(31) Li, W. L.; Wei, Z.; Zhu, K. J.; Wei, W. Q.; Yang, J.; Jing, J. F.; Phillips, D.; Zhu, Y. F. Nitrogen-defect induced trap states steering electron-hole migration in graphite carbon nitride. *Appl. Catal. B* **2022**, *306*, No. 121142.
(32) Wu, B. G.; Zhang, L. P.; Jiang, B. J.; Li, Q.; Tian, C. G.; Xie, Y.; Li, W. Z.; Fu, H. G. Ultrathin porous carbon nitride bundles with an adjustable energy band structure toward simultaneous solar photocatalytic water splitting and selective phenylcarbinol oxidation. *Angew. Chem., Int. Ed.* **2021**, *60*, 4815−4822.
(33) Qian, Y. Y.; Li, D. D.; Han, Y. L.; Jiang, H. L. Photocatalytic molecular oxygen activation by regulating excitonic effects in covalent organic frameworks. *J. Am. Chem. Soc.* **2020**, *142*, 20763−20771.
(34) Ghosh, I.; Khamrai, J.; Savateev, A.; Shlapakov, N.; Antonietti, M.; König, B. Organic semiconductor photocatalyst can bifunctionalize arenes and heteroarenes. *Science* **2019**, *365*, 360−366.
(35) Li, J.; Cui, W.; Sun, Y.; Chu, Y.; Cen, W.; Dong, F. Directional electron delivery via a vertical channel between g-C_3N_4 layers promotes photocatalytic efficiency. *J. Mater. Chem. A* **2017**, *5*, 9358−9364.
(36) Cui, W.; Li, J. Y.; Cen, W. L.; Sun, Y. J.; Lee, S. C.; Dong, F. Steering the interlayer energy barrier and charge flow via bioriented transportation channels in g-C_3N_4: Enhanced photocatalysis and reaction mechanism. *J. Catal.* **2017**, *352*, 351−360.
(37) Tian, S.; Fu, Q.; Chen, W.; Feng, Q.; Chen, Z.; Zhang, J.; Cheong, W. C.; Yu, R.; Gu, L.; Dong, J.; Luo, J.; Chen, C.; Peng, Q.; Draxl, C.; Wang, D.; Li, Y. Carbon nitride supported Fe_2 cluster catalysts with superior performance for alkene epoxidation. *Nat. Commun.* **2018**, *9*, 2353.
(38) Li, J. S.; Li, S. L.; Tang, Y. J.; Han, M.; Dai, Z. H.; Bao, J. C.; Lan, Y. Q. Nitrogen-doped Fe/Fe_3C@graphitic layer/carbon nanotube hybrids derived from MOFs: efficient bifunctional electrocatalysts for ORR and OER. *Chem. Commun.* **2015**, *51*, 2710−2713.
(39) Chen, L.; Wang, Y. X.; Cheng, S.; Zhao, X. L.; Zhang, J. Q.; Ao, Z. M.; Zhao, C. C.; Li, B.; Wang, S. J.; Wang, S. B.; Sun, H. Q. Nitrogen defects/boron dopants engineered tubular carbon nitride for efficient tetracycline hydrochloride photodegradation and hydrogen evolution. *Appl. Catal. B* **2022**, *303*, No. 120932.
(40) Lai, J. K.; Wachs, I. E. A perspective on the selective catalytic reduction (SCR) of NO with NH_3 by Supported V_2O_5−WO_3/TiO_2 Catalysts. *ACS Catal.* **2018**, *8*, 6537−6551.
(41) Zhang, G. G.; Li, G. S.; Lan, Z. A.; Lin, L. H.; Savateev, A.; Heil, T.; Zafeiratos, S.; Wang, X. C.; Antonietti, M. Optimizing Optical Absorption, Exciton Dissociation, and Charge Transfer of a Polymeric Carbon Nitride with Ultrahigh Solar Hydrogen Production Activity. *Angew. Chem., Int. Ed.* **2017**, *56*, 13445−13449.
(42) Chen, J. Y.; Qin, C. C.; Mou, Y.; Cao, Y. X.; Chen, H. Y.; Yuan, X. Z.; Wang, H. Linker regulation of iron-based MOFs for highly effective Fenton-like degradation of refractory organic contaminants. *Chem. Eng. J.* **2023**, *459*, No. 141588.
(43) Yang, R. Q.; Song, G. X.; Wang, L. W.; Yang, Z. W.; Zhang, J.; Zhang, X.; Wang, S.; Ding, L. H.; Ren, N.; Wang, A. Z.; Yu, X. Full solar-spectrum-driven antibacterial therapy over hierarchical Sn_3O_4 /PDINH with enhanced photocatalytic activity. *Small* **2021**, *17*, No. 2102744.
(44) Li, J.; Dong, X.; Sun, Y.; Cen, W.; Dong, F. Facet-dependent interfacial charge separation and transfer in plasmonic photocatalysts. *Appl. Catal. B* **2018**, *226*, 269−277.

https://doi.org/10.1021/acsomega.3c02654
ACS Omega 2023, 8, 27276−27283